

Optimizing Biophysically-Plausible Large-Scale Circuit Models With Deep Neural Networks

Tianchu Zeng^{1,2,3,*}, Fang Tian^{1,2,3,*}, Shaoshi Zhang^{1,2,3,4}, Gustavo Deco^{5,6}, Theodore Satterthwaite^{7,8,9}, Avram Holmes^{10,11}, B.T. Thomas Yeo^{1,2,3,4,12,13}

¹Centre for Sleep & Cognition & Centre for Translational Magnetic Resonance Research, Yong Loo Lin School of Medicine, National University of Singapore, Singapore;

²Department of Electrical and Computer Engineering, National University of Singapore, Singapore; ³N.1 Institute for Health, National University of Singapore, Singapore;

⁴Integrative Sciences and Engineering Programme (ISEP), National University of Singapore, Singapore; ⁵Center for Brain and Cognition, Department of Technology and Information,

Universitat Pompeu Fabra, Barcelona, Spain; ⁶Institució Catalana de la Recerca i Estudis Avançats, Universitat Barcelona, Barcelona, Spain; ⁷Penn Lifespan Informatics and Neuroimaging Center, University of Pennsylvania, Philadelphia, PA 19104, USA;

⁸Department of Psychiatry, University of Pennsylvania, Philadelphia, PA 19104, USA;

⁹Lifespan Brain Institute (LiBI) of Penn Medicine and CHOP, University of Pennsylvania, Philadelphia, PA 19104, USA; ¹⁰Department of Psychiatry, Brain Health Institute, Rutgers University, Piscataway, NJ, United States; ¹¹Center for Advanced Human Brain Imaging

Research, Rutgers University, Piscataway, NJ, United States; ¹²Department of Medicine, Healthy Longevity Translational Research Programme, Human Potential Translational

Research Programme & Institute for Digital Medicine (WisDM), Yong Loo Lin School of Medicine, National University of Singapore, Singapore; ¹³Athinoula A. Martinos Center for

Biomedical Imaging, Massachusetts General Hospital, Charlestown, USA

* equal contributions

Address correspondence to:

B.T. Thomas Yeo

CSC, TMR, ECE, N.1, WISDM

National University of Singapore

Email: thomas.yeo@nus.edu.sg

Abstract

Biophysically plausible large-circuit models provide valuable mechanistic insights into neural dynamics. However, setting up a model involves numerous free parameters, which are often manually set, leading to assumptions that may not align with biological plausibility. In contrast, optimizing these parameters results in more biologically plausible models. Previous papers have shown that spatially heterogeneous parameters improve the model performance in generating realistic neural dynamics. Prior works have employed iterative forward simulations via Euler integration to optimize the parameters, which require solving ordinary differential equations (ODE) for all regions simultaneously and each time step sequentially. This process poses a computational hurdle for an efficient model inversion. To tackle this problem, we propose DELSSOME (Deep Learning for Surrogate Statistics Optimization in Mean Field Modeling), which integrates deep learning models into neural mass model framework to circumvent the need to solve ODEs. These deep learning models are designed to learn surrogate statistics, which directly provide outputs required for optimization, from the input local circuit parameters. Our experiments demonstrate that our approach leads to a remarkable 500,000% speed-up of parameter optimization process compared to the traditional approach while achieving comparable performances. Moreover, our approach successfully replicates previous findings on excitation-inhibition ratio changes related to neurodevelopment and cognition. Overall, our results suggest the efficiency and broader applicability of the proposed approach in uncovering intricate neural dynamics.

1 Introduction

Large-scale biophysically plausible models of coupled brain regions are developed to provide mechanistic insights into spontaneous brain dynamics (Honey et al., 2007; Ghosh et al., 2008; Shine et al., 2021; Singh et al., 2020; Zalesky et al., 2014). For instance, in fMRI datasets, previous works have shown that some models elucidate how resting-state functional connectivity (FC) arises from anatomical connections and how the balance of local excitation and inhibition influences global brain dynamics (Deco et al., 2013, 2014; Demirtaş et al., 2019).

However, leveraging these models to extract biological insights necessitates meticulous parameter optimization (Kong et al., 2021; S. Zhang et al., 2024). Typically, parameters are manually set, often through methods like grid searching across predefined ranges (Ghosh et al., 2008; Honey et al., 2009; Deco et al., 2013). However, such approaches are limited to models with few parameters, like those models that assume parameters to be identical for all brain regions (Deco et al., 2014; Trakoshis et al., 2020; Lam et al., 2022), restricting their ability to capture complex biophysical information.

Capturing information across diverse brain regions requires heterogeneous parameters (Cardin et al., 2009; Burt et al., 2018; Huntenburg et al., 2018; Froudast-Walsh et al., 2021; Goulas et al., 2021). However, the parameter estimation process for heterogeneous models presents a significant challenge due to the computational burden associated with solving multiple coupled ordinary differential equations (ODEs) (Wang et al., 2019; Kringelbach & Deco, 2020; Deco et al., 2021; Kong et al., 2021; S. Zhang et al., 2024). The incorporation of heterogeneity significantly increases the number of ODEs and parameters, rendering traditional search methods impractical. Consequently, various algorithms are proposed for heterogeneous parameter optimization. As shown in prior works (Kong et al., 2021; S. Zhang et al., 2024), covariance matrix adaptation evolution strategy (CMA-ES) shows promising results (N. Hansen, 2006). However, this method often entails extensive iterations, with each iteration requiring computationally expensive Euler integration to simulate fMRI data for all cortical regions across multiple time steps. In other words, the computational burden of Euler integration is notable in both the spatial and temporal domains. Numerous regions of interest (ROIs) and a sufficiently small step size of Euler integration are required when using Euler integration to generate simulated fMRI data. As a result, Euler integration must be executed numerous times in both spatial and temporal domains, often numbering in the billions for a single iteration, which poses a substantial computational hurdle when optimizing parameters.

To overcome the limitation, we considered leveraging deep learning, renowned for its capability as a universal approximator, to accelerate the process of parameter optimization. In this work, we proposed DELSSOME (DEep Learning for Surrogate Statistics Optimization in MEan field modeling) models. This approach involved training deep learning models to learn surrogate statistics, which meant, specifically, the hidden representations of biophysical parameters. These surrogate statistics could then be used to bypass Euler integration, providing accurate loss terms for evolutionary algorithms to iterate efficiently.

To evaluate our approach, we started by exploring the efficacy of deep learning models in capturing surrogate statistics, employing the Human Connectome Project (HCP) S1200 release dataset (Glasser et al., 2013; Van Essen et al., 2013). The outcomes demonstrated strong performance, indicating that deep learning models can accurately capture surrogate statistics. These hidden representations could be directly leveraged to optimize parameters. In integrating these deep learning models into CMA-ES iterations, we adopted a new CMA-ES procedure called DELSSOME CMA-ES, enabling us to accelerate parameter optimization by 500,000% without compromising performance. Following this success, we validated our method's effectiveness using the Philadelphia Neurodevelopmental Cohort (PNC) dataset (Satterthwaite et al., 2014; Calkins et al., 2015), replicating previous findings regarding the Excitation/Inhibition (E/I) ratio during development and cognitive process (S. Zhang et al., 2024).

Our work offers several significant contributions. First, it demonstrates the capability of deep learning models to capture crucial surrogate statistics within large-scale biophysical models. This ability opens avenues for enhanced understanding and analysis of complex brain dynamics. Secondly, by leveraging these surrogate statistics, we accelerate parameter optimization in large-scale biophysical models. This acceleration streamlines the research process and holds the potential to expedite discoveries pertaining to brain dynamics, thus contributing to advancements in neuroscience research.

2 Methods

2.1 Datasets

2.1.1 Human Connectome Project (HCP) dataset

We considered 1029 participants from the Human Connectome Project (HCP) S1200 release (Glasser et al., 2013; Van Essen et al., 2013). These participants underwent scanning on a customized Siemens 3T Skyra using a multi-band sequence. Each participant completed four resting-state fMRI (resting-fMRI) runs in two sessions on two different days. The resting-fMRI runs had a repetition time (TR) of 0.72 s at 2 mm isotropic resolution, each lasting 14.4 minutes. Additionally, six runs of diffusion imaging were conducted, each lasting approximately 9 minutes and 50 seconds. Diffusion weighting consisted of 3 shells of b-values (1000, 2000, and 3000 s/mm²) with approximately equal number of weighting directions on each shell. Further specifics of the data collection are available elsewhere (Van Essen et al., 2013).

Preprocessing of the HCP data is detailed in the HCP S1200 manual. We utilized preprocessed (MSMAll) resting-fMRI data, already projected to fsLR surface space, denoised with ICA-FIX, and smoothed by 2 mm. For each run of each participant, the fMRI data were averaged within each Desikan–Killiany region of interest (ROI) (Desikan et al., 2006) to create a 68×1200 matrix. These matrices were used to compute 68×68 functional connectivity (FC) matrices by correlating the time courses among all pairs of time courses. FC matrices were then averaged across runs of participants within a particular group of participants to produce group-averaged FC matrices.

Functional connectivity dynamics (FCD) were computed by defining a 60-second window (equivalent to 83 time points or TRs) and sliding the window frame by frame, resulting in 1118 sliding windows (E. C. Hansen et al., 2015; Leonardi & Van De Ville, 2015). FC was computed within each sliding window for each participant's run. Each sliding window FC matrix was then vectorized by only considering the upper triangular entries. The vectorized FCs were correlated, resulting into a 1118×1118 FCD matrix. Unlike static FC, FCD matrices could not be directly averaged across participants due to the lack of temporal correspondence during resting-state.

For diffusion MRI, probabilistic tractography was conducted for each participant using the second-order integration over fiber orientation distribution (iFOD2) algorithm provided by MRtrix3 (Tournier et al., 2010; Tournier et al., 2019). The Anatomically-Constrained Tractography (ACT) (Smith et al., 2012) was performed on fiber orientation

distribution (FOD) images. 5,000,000 streamlines were sampled to generate tractograms, which were then filtered using Spherical-deconvolution informed filtering of tracks (SIFT2; Smith et al., 2015). This generated a structural connectivity (SC) matrix for each participant, where each entry represented the number of streamlines between two ROIs. To generate a group-level SC matrix, a thresholding procedure was first applied to remove false positives. More specifically, if <50% of participants had a non-zero value in a particular entry in the SC matrix, then the entry is set to zero in all individual-level SC matrices. Then averaging across participants with non-zero streamlines, log-transforming the averaged values, and setting the main diagonal entries to zero were performed. Group-level SCs were computed separately for a particular group of participants, with the maximum value normalized to 0.02.

2.1.2 Philadelphia Neurodevelopment Cohort (PNC) dataset

Neuroimaging data were acquired from a community-based cohort comprising 1601 youth aged 8.1 to 23.1 (mean = 14.94, standard deviation = 3.69, male/female = 764/837) enrolled in the Philadelphia Neurodevelopmental Cohort (PNC). Previous publications have provided comprehensive details regarding data collection procedures and participant demographics (Satterthwaite et al., 2014; Calkins et al., 2015). A single resting-fMRI scan was collected from each participant. Consistent with our previous work, after excluding individuals based on health criteria and stringent quality control measures, a total of 885 participants (aged 8.2 to 23.0 at initial visit, mean = 15.66, standard deviation = 3.36) were retained (Zhang et al., 2024).

All neuroimaging data were acquired using the Siemens Trio 3T scanner, with detailed descriptions of imaging protocols and acquisition parameters available elsewhere. In brief, parameters included TR = 3000 ms, TE = 32 ms, flip angle = 90°, FOV = 192 × 192 mm², matrix = 64 × 64, 46 slices, slice thickness/gap = 3/0 mm, effective voxel resolution = 3.0 × 3.0 × 3.0 mm³, and a total of 210 volumes.

BOLD runs were slice time-corrected and then motion-corrected. Susceptibility distortion was estimated and used to compute a corrected BOLD reference for more accurate co-registration with the anatomical reference. The BOLD reference was co-registered to the T1w reference using boundary-based registration. Co-registration was configured with nine degrees of freedom to account for distortions remaining in the BOLD reference. Six head motion parameters (corresponding rotation and translation parameters) were estimated before any spatiotemporal filtering. The motion-correcting transformations and field distortion

correcting warp were applied to the BOLD time series in a single step. Finally, the volumetric data was projected to fsaverage6 surface space.

Nuisance regression incorporated anatomical CompCor (aCompCor), with principal components estimated after high-pass filtering of preprocessed BOLD time series (using a discrete cosine filter with a 128-s cutoff). Five CompCor components were extracted from cerebrospinal fluid (CSF) and white matter (WM) masks. In total, 17 regressors were jointly regressed from the BOLD time series, including 6 head motion parameters and their temporal derivatives, and top 5 aCompCor components.

FC and FCD for the PNC datasets were computed in the same manner as the HCP dataset. However, due to a longer TR in the PNC dataset compared to the HCP dataset, the length of each sliding window for FCD matrix computation was set to 20 timepoints (or TRs) to maintain a consistent window length of 60 seconds.

2.2 Parametric feedback inhibition control (pFIC) model

Given the instantiation of the FIC model using the Desikan-Killiany parcellation with 68 ROIs, achieving spatial heterogeneity for local circuit parameters w_{EE} , w_{EI} , σ (with G being a global constant) presented computational challenges. Direct optimization of each parameter independently would entail handling a total of $68 \times 3 + 1 = 205$ parameters. To tackle this problem, following our prior work (Kong et al., 2021; S. Zhang et al., 2024), we reduced the number of “free” parameters by parameterizing the local circuit parameters with a linear combination of the first principal FC gradient (Margulies et al., 2016) and T1w/T2w ratio map (Glasser & Van Essen, 2011).

$$w_{EE,j} = a + b \times \text{T1w/T2w ratio}_j + c \times \text{FC gradient}_j \quad (7)$$

$$w_{EI,j} = d + e \times \text{T1w/T2w ratio}_j + f \times \text{FC gradient}_j \quad (8)$$

$$\sigma_j = g + h \times \text{T1w/T2w ratio}_j + i \times \text{FC gradient}_j \quad (9)$$

where j denotes the ROI index. By employing this parameterization strategy, the number of “free” numbers was reduced to $3 \times 3 + 1 = 10$ parameters.

2.3 Local circuit parameter optimization by CMA-ES

Following our prior work (S. Zhang et al., 2024), covariance matrix adaptation evolution strategy (CMA-ES) (N. Hansen, 2006) was used to iteratively optimize local circuit parameters (**Figure 1A**). CMA-ES is an optimization technique used to find the best solution to complex problems by iteratively testing and improving potential solutions. It works by

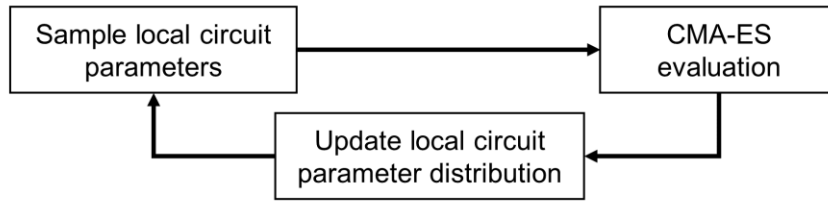
generating a group of candidates (solutions) and evaluating how well they perform. In each iteration, based on the performance of candidates, CMA-ES adjusts the "search direction" by learning which directions in the search space are most promising. In our case, it started with sampling 100 candidate local circuit parameters from an initialized Gaussian distribution. Simulated fMRI data were generated by running Euler forward simulations with local circuit parameters and structural connectivity (SC) matrices. After evaluation, 10 candidate parameters with best performance were used to update the sampling distribution for the next iteration.

Evaluation of candidate parameters was based on the similarity between simulated and empirical fMRI data. The simulated fMRI data with firing rates outside the physiologically plausible range of 2.7 ~ 3.3 Hz (De Kock & Sakmann, 2008) were filtered out. For the remaining simulated fMRI data, given the inherent difficulty in directly measuring the similarity of two time series, we opted to quantify agreement through the comparison of extracted features from fMRI, specifically focusing on static functional connectivity (FC) and FC dynamics (FCD). We quantified the agreement between empirical and simulated FC using Pearson's correlation (r) and absolute difference between the means (d) (Demirtaş et al., 2019), as well as empirical and simulated FCD using KS statistics (KS). Parameters with the minimum loss, defined as $(1-r) + d + KS$, were used to initialize candidate parameters for the next iteration (**Figure 1B**). To alleviate the computational burden associated with Euler forward simulation in generating simulated fMRI data, we sought to integrate deep learning models into our workflow. Our objective was to develop models capable of effectively replacing Euler forward simulation. These models could identify and filter out parameter sets likely to generate simulated fMRI data outside of a predefined firing rate range (De Kock & Sakmann, 2008; Wilson et al., 1994). Additionally, these models needed to output loss metrics for updating CMA-ES iteration parameters. To fulfill these requirements, we designed two components: the DELSSOME out-of-range classifier and the DELSSOME loss predictor. Upon acquiring trained DELSSOME out-of-range classifier and DELSSOME loss predictor models, we could streamline and expedite the evaluation process, which was referred to as DELSSOME CMA-ES evaluation procedure (**Figure 1C**). After sampling 100 candidate local circuit parameter from a distribution, it involved a two-step procedure. First, the DELSSOME out-of-range classifier was utilized to identify and filter out parameter sets likely to yield fMRI data with firing rates outside the physiologically plausible range of 2.7 ~ 3.3 Hz (De Kock & Sakmann, 2008). This range was grounded in previous research indicating typical firing rates of excitatory neurons in the human brain cortex during

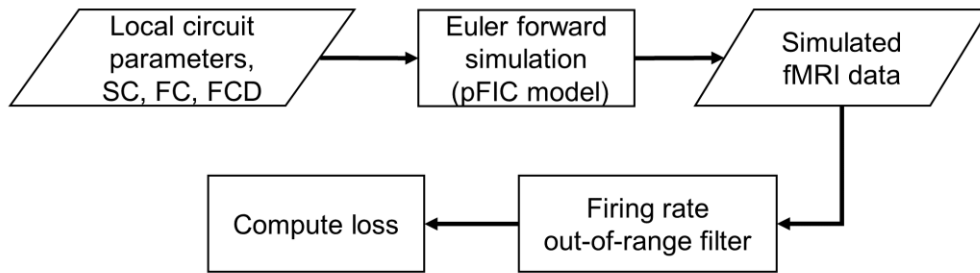
resting state. Subsequently, the DELSSOME loss predictor directly predicted the three loss terms ($1-r$, d , KS). 10 parameters with the lowest loss are used for the initialization of candidate parameters distribution for subsequent iterations.

2.4 Data generation

(A) CMA-ES workflow



(B) CMA-ES evaluation (Euler)



(C) CMA-ES evaluation (DELSSOME)



Figure 1. CMA-ES workflow and evaluation procedures. (A) CMA-ES workflow. Local circuit parameters are sampled from an initial distribution. The local circuit parameters are then evaluated either using Euler approach or DELSSOME approach. The parameters with the lowest loss are used to update the sampling distribution. (B) CMA-ES evaluation (Euler). For input local circuit parameters and structural connectivity (SC), Euler forward simulation applied to pFIC model is used to generate simulated fMRI data. After filtering out simulated fMRI data with firing rate outside the range, we compute the corresponding loss with empirical functional connectivity (FC), FC Dynamics (FCD) for remaining simulated fMRI data. Parallelograms denote input/output, while rectangles denote operations. (C) CMA-ES evaluation (DELSSOME). Input local circuit parameters and structural connectivity, the DELSSOME out-of-range classifier first filters out local circuit parameters that would generate simulated fMRI data with firing rate that are outside the firing rate range. The

DELSSOME loss predictor then predicts the loss regarding the remaining local circuit parameters with empirical FC and FCD directly from parameters without solving the ODEs.

In our study, we utilized HCP dataset to generate the training, validation, and test set for DELSSOME out-of-range classifier and DELSSOME loss predictor (**Figure 2**).

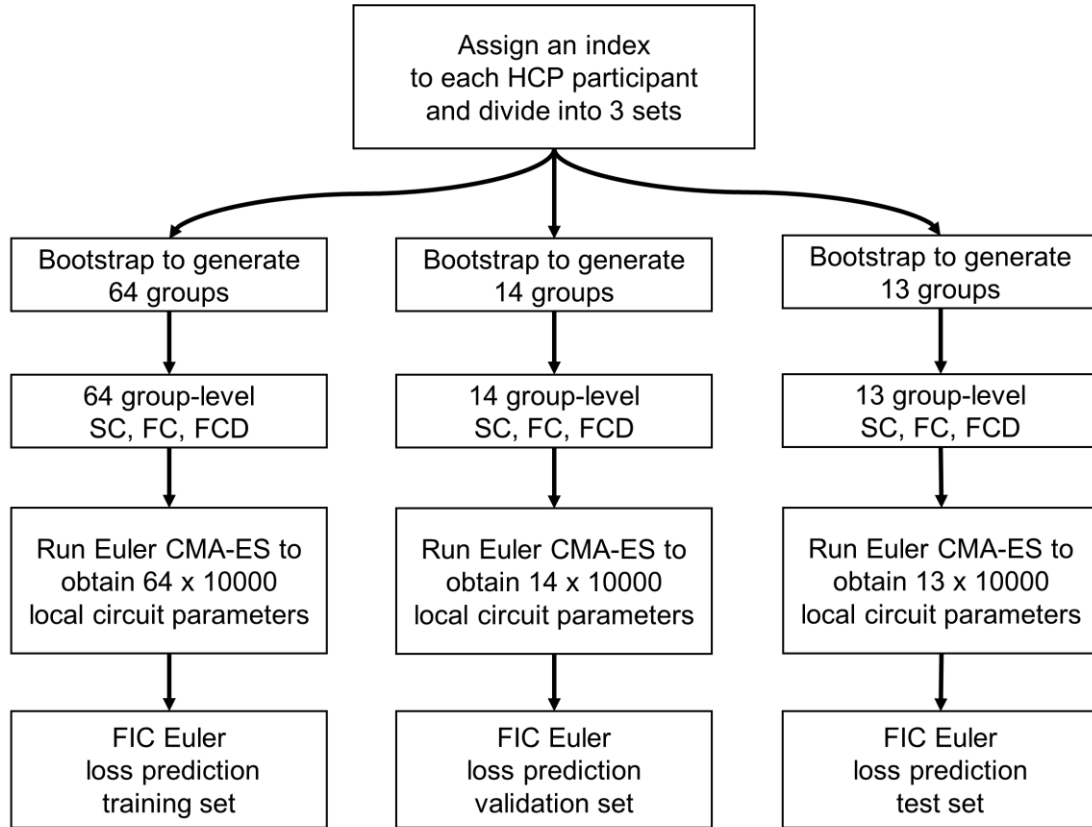


Figure 2. Deep learning data generation for out-of-range firing rate classification as well as empirical-fMRI and simulated-fMRI discrepancy prediction. HCP dataset is used for deep learning models training, validation and test processes. We group participants and use Euler CMA-ES to generate FIC Euler loss prediction training, validation and test set respectively.

We partitioned the dataset, comprising 1029 participants, into three non-overlapping sets: a training set with 680 participants, a validation set with 180 participants, and a test set with 169 participants. Each set underwent further grouping into numerous subgroups. Specifically, structural connectivity (SC), functional connectivity (FC), and functional connectivity dynamics (FCD) matrices from 50 participants were grouped together. To generate group-level SC, FC, and FCD matrices, we employed bootstrapping techniques, resulting in 64 group-level SC, FC and FCD matrices for the training set, 14 for the validation set, and 13 for the test set. To implement the bootstrapping technique in our study,

we employed a sliding-window approach. This approach involved grouping participants by sliding a window across the dataset. The process mainly consisted of two steps. Initially, participants in the dataset were numbered sequentially. Secondly, to form each group, we selected a subset of participants by sliding a window across the dataset. For example, the first group comprised participants numbered 1 to 50, the second group comprised participants numbered 10 to 60, and so forth. Essentially, we moved the window by a fixed increment (e.g., 10 participants) to create overlapping subsets of participants.

Subsequently, utilizing these grouped matrices, we employed traditional CMA-ES with Euler evaluation procedures to generate local circuit parameters. During this process, two key factors were recorded for each group: firstly, whether the local circuit parameters yielded fMRI data within the specified firing rate range, and secondly, the corresponding values of the three loss terms ($1-r$, d , KS) if the simulated firing rates were within the specified range.

For each group in the training/validation/test set, we generated 10,000 sets of local circuit parameters along with their associated records. Consequently, we obtained a total of 640,000 local circuit parameter sets with corresponding records in the training set, 140,000 in the validation set, and 130,000 in the test set. These local circuit parameters, together with their corresponding records and group-level SC, FC, and FCD matrices, constituted the training, validation, and test sets for FIC Euler loss prediction, respectively.

2.5 Deep learning models architecture

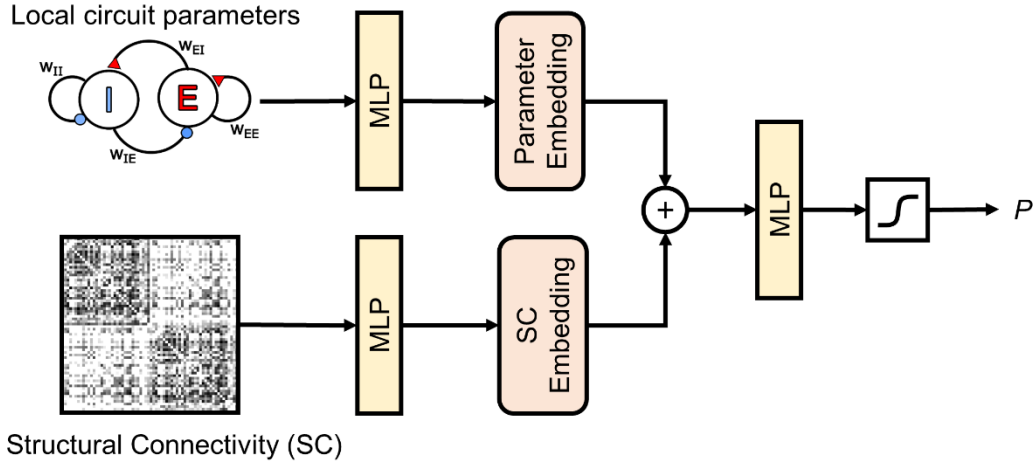
Our deep learning models consisted of two components: a DELSSOME out-of-range classifier and a DELSSOME loss predictor. The DELSSOME out-of-range classifier could identify and filter out parameter sets likely to generate simulated fMRI data outside of a predefined firing rate range. The DELSSOME loss predictor could output loss metrics for updating CMA-ES iteration parameters.

The architecture of DELSSOME out-of-range classifier is shown in **Figure 3A**. The model inputs were the local circuit parameter and the structural connectivity (SC) matrix. Utilizing a multilayer perceptron (MLP) module, the local circuit parameter underwent transformation into a parameter embedding, while another MLP module processed the SC matrix to generate a corresponding SC embedding. These embeddings served as surrogate statistics encapsulating the essential information from the local circuit parameter and SC matrix. By combining these embeddings and passing them through an additional MLP layer, the model “read out” the surrogate statistics, ultimately outputting the probability that the

given pair of local circuit parameter and SC will yield fMRI data outside our predefined firing rate range. During application, if this probability exceeded 50%, the respective local circuit parameter would be filtered out.

The architecture of the DELSSOME loss predictor (**Figure 3B**) was designed to accommodate the prediction of three loss terms, necessitating the inclusion of empirical functional connectivity (FC) and functional connectivity dynamics (FCD) data. Similar to the DELSSOME out-of-range classifier, this model incorporated MLPs to generate embeddings for the local circuit parameter and SC. Additionally, MLP modules were employed to produce FC and FCD embeddings from empirical FC and FCD data, respectively. For generating surrogate statistics related to loss terms $1-r$ and d , the embeddings of the local circuit parameter, SC, and empirical FC were combined and passed through a MLP layer to output these terms. Similarly, surrogate statistics for loss term KS were generated by combining the embeddings of the local circuit parameter, SC, and empirical FCD, followed by passing through a MLP to estimate the KS loss.

(A) DELSSOME out-of-range classifier



(B) DELSSOME loss predictor

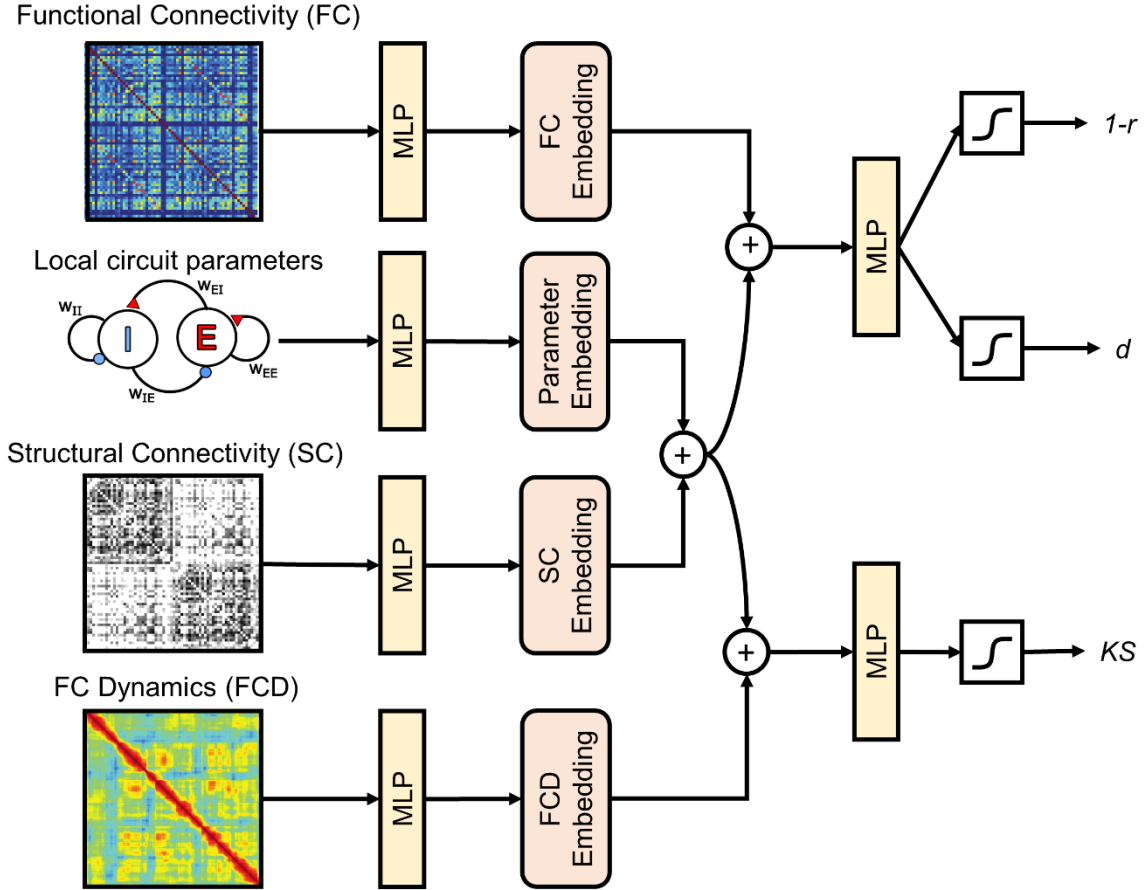


Figure 3. DELSSOME Model architectures. (A) Model overview of the DELSSOME out-of-range classifier. The inputs to this model are local circuit parameters and structural connectivity. We add these embeddings to predict the probability (P) of the parameter to

simulate fMRI data within firing rate constraint. (B) Model overview of the DELSSOME loss predictor. The inputs to this model are local circuit parameters, structural connectivity, static and dynamic functional connectivity. We add these embeddings to predict the disagreement between empirical and simulated fMRI data. We quantify the agreement between empirical and simulated FC using Pearson correlation (r) and absolute difference between the means (d), as well as empirical and simulated FCD using KS statistics (KS). Note that FCD input is the cumulative sum of the distribution of FCD entries (FCD-CDF).

2.6 Benchmarking

In order to validate the trained DELSSOME out-of-range classifier and DELSSOME loss predictor, we compared the performance and computational efficiency in the context of parameter optimization from two distinct methods:

- **Euler CMA-ES:** This method involved 100 iterations of the CMA-ES, utilizing the Euler evaluation procedure as illustrated in **Figure 1B**.
- **DELSSOME CMA-ES:** Similarly, this method employed 100 iterations of CMA-ES, but instead utilized the evaluation procedure outlined in **Figure 1C**, incorporating the trained DELSSOME out-of-range classifier and DELSSOME loss predictor.

These methods were applied to the FIC Euler loss prediction test set participants ($N = 169$) for comparative analysis (**Figure 4**). To facilitate evaluation, the test set participants were further divided into three subsets, which we termed FIC inversion training/validation/test sets. We generated the group-level SC, FC, and FCD for each set. Euler/DELSSOME CMA-ES were applied to the training set to optimize local circuit parameters. For each algorithm, we employed 50 different initializations for a more robust comparison.

In the validation phase, the local circuit parameter with the lowest training loss in each training iteration was selected and fed into the FIC inversion validation set. This process yielded a total of 100 candidate local circuit parameters for validation and Euler simulation was used to generate simulated BOLD time series for each of these local circuit parameters. The parameter with the minimum validation loss was utilized in the test set for the assessment of test loss.

Through this comparative analysis, we aimed to elucidate the relative performance and efficiency of the Euler and DELSSOME CMA-ES methods in the context of parameter optimization.

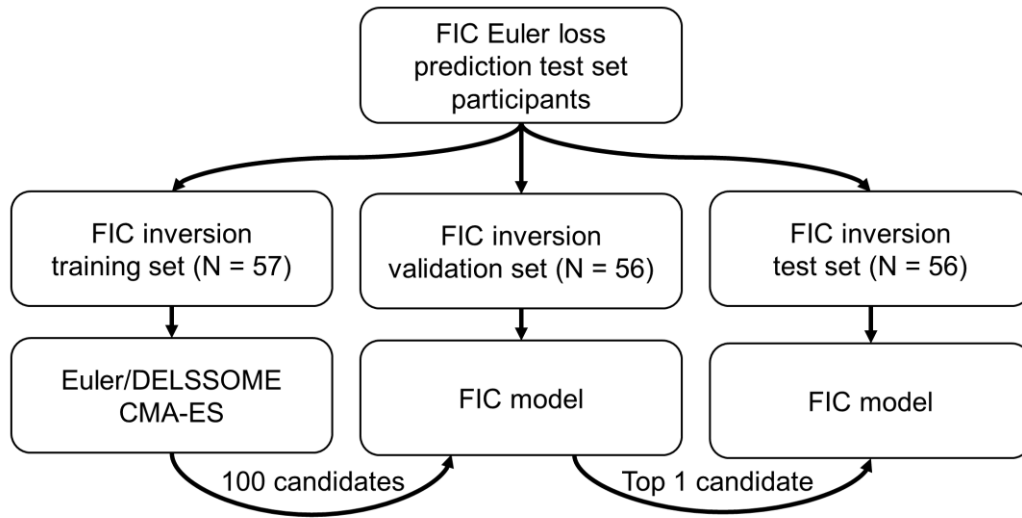


Figure 4. HCP Feedback Inhibition Control (FIC) model parameter estimation workflow. We split the HCP FIC Euler loss prediction test set participants into the FIC inversion training, validation, test set. We used two different methods (i.e., Euler CMA-ES, DELSSOME CMA-ES) to train local circuit parameters.

2.7 PNC replication and analysis

To validate the ability of the DELSSOME models to capture neuroscientific information, we utilized the PNC dataset, aiming to replicate our previous findings regarding the development of the excitatory/inhibitory (E/I) ratio and its association with cognitive processes via Euler CMA-ES (Larsen et al., 2022; S. Zhang et al., 2024).

The data used were the same as those in our previous paper (S. Zhang et al., 2024). Following data preprocessing and quality control, our sample consisted of 885 participants aged 8-23 years old. To replicate previous E/I ratio development findings, participants were stratified into 29 age groups, each comprising approximately 30-31 participants. Within each age group, 15 participants were randomly allocated to the validation set, while the remaining participants were assigned to the training set. The SC matrix used was grouped from HCP FIC Euler loss prediction training set and remained the same for each group.

For each age group, we employed the DELSSOME or Euler CMA-ES, comprising 100 iterations of DELSSOME or 50 iterations of Euler evaluation procedure to optimize model parameters. Subsequently, 500 (250 for Euler CMA-ES) candidate parameter sets were generated from the training set and evaluated in the validation set. The parameter set exhibiting the lowest validation cost was utilized to estimate regional E/I ratios across the cortex.

Regarding cognitive processes, participants in the PNC dataset completed the Penn Computerized Neurocognitive Battery (CNB), yielding an overall accuracy measure as well as domain-specific factor scores. Participants were categorized into 14 high-performance and 14 low-performance groups based on overall accuracy, with each high-performance group age-matched to a low-performance group. Each group comprised approximately 31-32 participants, with 15 participants randomly assigned to the validation set and the remainder to the training set. The SC matrix used was grouped from HCP FIC Euler loss prediction training set and remained the same for each group.

For each cognitive performance group, the DELSSOME CMA-ES approach, incorporating 100 DELSSOME or 50 Euler iterations, was employed to optimize parameters. Subsequently, 500 (250 for Euler) candidate parameter sets were generated from the training set, and the top-performing set from the validation set was utilized to estimate the E/I ratio. Finally, we compared the E/I ratios between the high- and low-performance groups to assess their association with cognitive functioning.

Through this comprehensive analysis, we aimed to validate the DELSSOME models' capacity to capture neuroscientific phenomena and their potential utility in elucidating the relationship between neural dynamics and cognitive processes.

3 Results

3.1 Deep learning models capture surrogate statistics for parameter optimization

To speed up the parameter optimization process, particularly to circumvent the computational burden associated with Euler forward simulation in large-scale biophysically plausible models, we explored the utilization of deep learning neural networks to learn compressed representations of essential components: local circuit parameters, structural connectivity (SC), static functional connectivity (FC), and functional connectivity dynamics (FCD). These compressed representations, termed surrogate statistics, served as proxies for the original matrices and could be leveraged to infer the loss terms required for CMA-ES iterations.

The necessity for these matrices arised from the architecture of our large-scale biophysically plausible model. In this model, local circuit parameters and SC matrices were used to generate fMRI data. FC and FCD were used to measure the similarity between simulated and empirical fMRI data. While FC matrices could capture intrinsic information embedded within fMRI data, they inherently lacked the capacity to capture temporal features. To address this limitation, we utilized FCD matrices, which encapsulated the correlations between numerous sliding window FC matrices over time. By incorporating both FC and FCD matrices, we could effectively capture both spatial and temporal aspects of fMRI data, enabling a more comprehensive assessment of similarity between simulated and empirical fMRI data.

Two different deep learning models, implemented with Pytorch (Paszke et al., 2019), were used in our work. The DELSSOME out-of-range classifier was designed to capture the surrogate statistics from structural connectivity (SC) and local circuit parameters, to predict the firing rate information, in order to filter out those parameters that were likely to generate fMRI data with firing rate outside a predefined range. In other words, it assessed the likelihood that a given pair of local circuit parameters and SC will yield fMRI data within a predefined firing rate range. In our neural mass model the firing rate range aligned with experimental observations of excitatory neurons (2.7 ~ 3.3Hz) (De Kock & Sakmann, 2008). Meanwhile, the DELSSOME loss predictor integrated the information of SC, local circuit parameters, and empirical static functional connectivity (FC) and FC dynamics (FCD), to directly generate the loss between simulated and empirical matrices bypassing the process of solving the system ODE, thus speeding up the parameter optimization process.

Specifically, as shown in the previous study, evaluation of simulated fMRI data depended on the agreement between the empirical and simulated static functional connectivity (FC) and FC dynamics (FCD). We quantified the agreement between empirical and simulated FC using Pearson's correlation (r) and absolute difference between the means (d), as well as empirical and simulated FCD using KS statistics (KS). The DELSSOME loss predictor outputted three loss metrics ($1-r$, d , KS) between simulated and empirical FC and FCD, incorporating local circuit parameters, SC, and empirical data.

In our experiments, HCP participants were divided into three sets, FIC Euler loss prediction training/validation/test set. Within each set we grouped the SC, FC, FCD data of 50 participants together, and employed bootstrapping techniques to generate multiple groups. Specifically, 64 groups for training, 14 groups for validation and 13 groups for testing. The Desikan–Killiany anatomical parcellation (Desikan et al., 2006) with 68 cortical regions of interest (ROIs) was used to generate SC, FC and FCD matrices. Traditional parameter optimization approach (Euler CMA-ES) was employed to generate 10000 local circuit parameters for each group.

In the test set, the DELSSOME out-of-range classifier achieved an accuracy of 90.12%, largely above chance (60.88% of the parameters are inside range). This meant the compressed representation of local circuit parameters and SC contains enough information about firing rate, indicating its ability to capture surrogate statistics relevant to firing rates in the neural mass model.

The test results shown by DELSSOME loss predictor demonstrated close agreement with ground-truth loss values (**Figure 5A-5C**, $r > 0.9$), indicating its efficacy in capturing surrogate statistics not only from local circuit parameters but also from empirical FC and FCD data. We obtained similar results utilizing a 100-region homotopic parcellation (Figure S1) (Yan et al., 2023). These findings highlighted the potential of deep learning integration to streamline parameter estimation processes in biophysically realistic large scale models, facilitating more efficient and accurate investigations into brain dynamics.

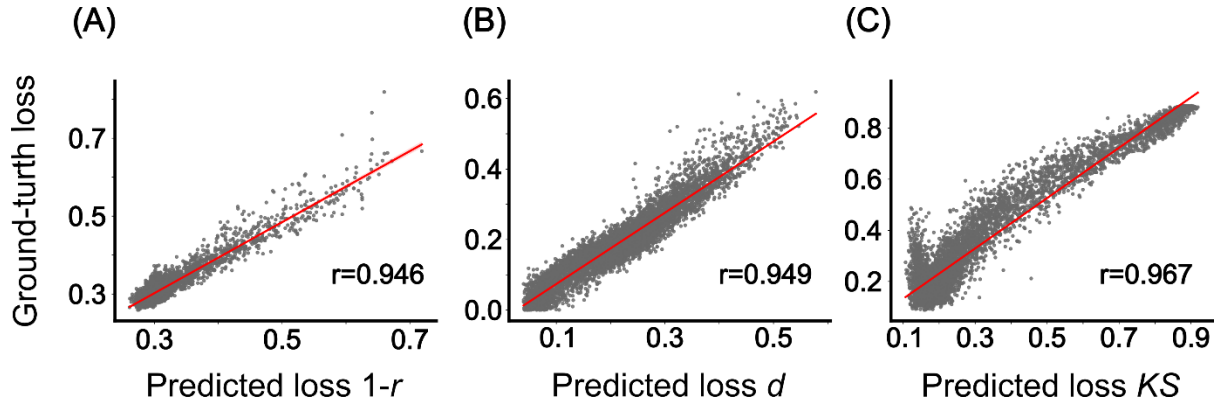


Figure 5. Model validation of DELSSOME loss predictor. (A)-(C) The plots show the model performance on one example test set. The horizontal axis shows the predicted loss, while the vertical axis shows the ground-truth loss. The correlation between the predicted and ground-truth loss are all above 0.9.

3.2 DELSSOME CMA-ES can generate comparable fMRI data while being 500,000% faster

To validate the real application of DELSSOME models in the context of parameter optimization, we split the FIC Euler loss prediction test set participants into three subsets, FIC inversion training/validation/test set, in order to compare the parameter optimization results of Euler CMA-ES and DELSSOME CMA-ES.

Following the training of the DELSSOME out-of-range classifier and loss predictor, a straightforward application of these models was to bypass Euler forward simulation in each iteration of Covariance Matrix Adaptation Evolution Strategy (CMA-ES) (N. Hansen, 2006), which could result in a remarkable speed up of parameter optimization procedure. In our experiments, Euler CMA-ES consisted of 100 iterations of forward simulation via Euler integration (Figure 1B), while DELSSOME CMA-ES was comprised of 100 iterations of DELSSOME evaluation process (Figure 1C).

Results indicated that using DELSSOME CMA-ES for optimization could offer a significant speed-up (Figure 6A, 500,000% speed-up) compared to Euler CMA-ES. Moreover, the optimized parameters by DELSSOME CMA-ES even numerically outperforms those by Euler CMA-ES using 50 different random initializations each (Figure 6B). The different initializations are used to demonstrate the robustness of DELSSOME CMA-ES. Similar results were shown by using the 100-region homotopic parcellation (Figure S2).

To further dig into the optimization procedure of DELSSOME CMA-ES, we utilized Euler integration to check the loss of parameters optimized for each iteration of DELSSOME CMA-ES in the validation set. The total validation loss generated using the Euler integration

showed a clear trend of decline (Pearson $r = -0.57$, average across 50 initializations), indicating a clear optimization trend of parameters. An example figure was shown (Figure S5).

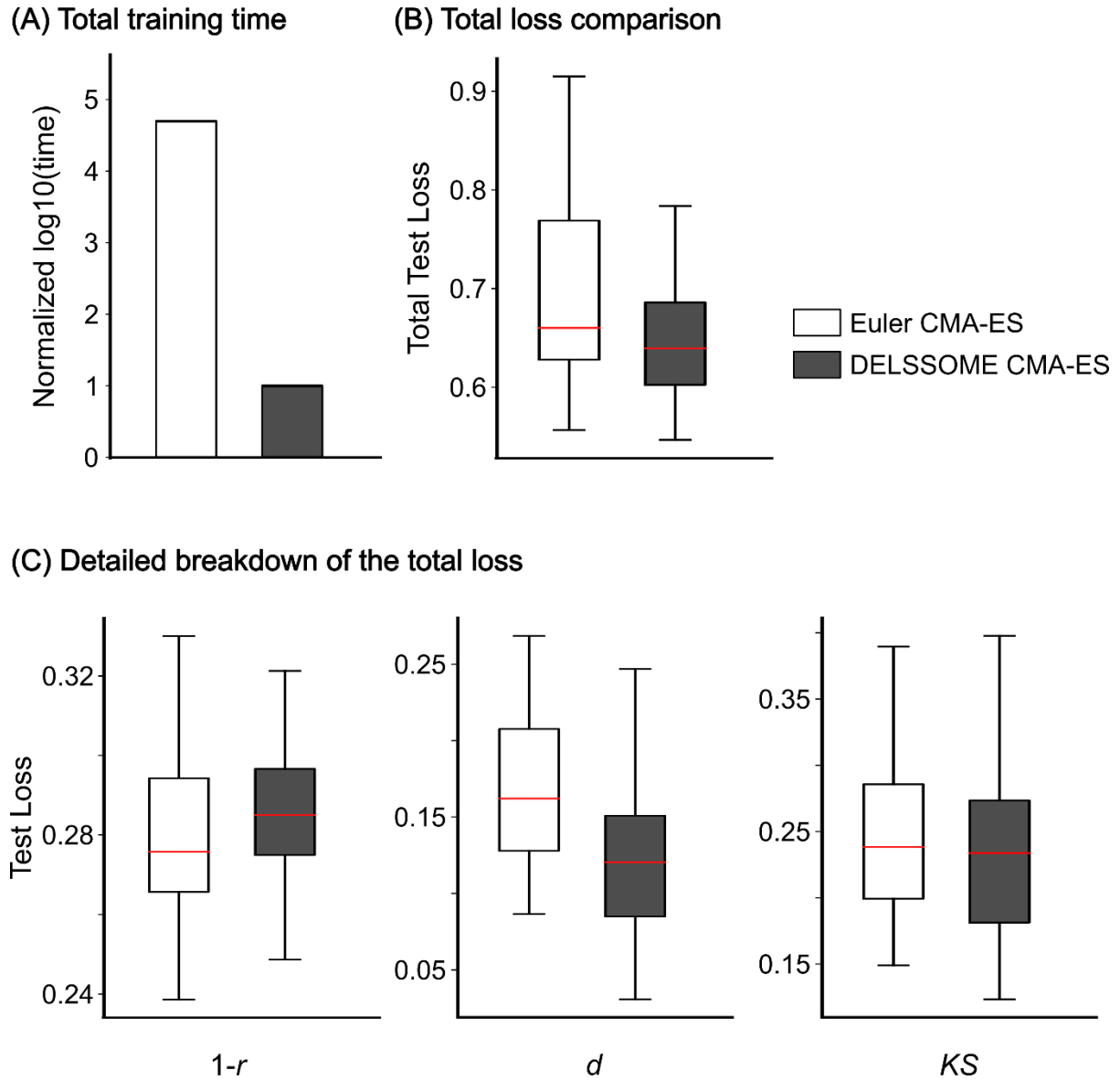


Figure 6. Two CMA-ES procedure comparison. (A) Time taken during model training. The bar plot shows the normalized log scale computational time taken during training for each approach. DELSSOME CMA-ES offers a 500,000% speed-up compared to traditional Euler CMA-ES. (B) Total Test Loss comparison. These boxplots contain 50 points each. Each point corresponds to the parameter set with the lowest total validation loss of 50 different random initializations. DELSSOME CMA-ES even outperforms Euler CMA-ES numerically. (C) Detailed breakdown of the total loss. The three losses all show comparable results that is similar to the pattern shown in total loss.

3.3 DELSSOME CMA-ES replicates previous findings of E/I ratio changes related to development and cognition

To validate the effectiveness of the DELSSOME CMA-ES approach in retaining neuroscientific information in the parameter optimization process, we tried replicating our prior investigations on the dynamics of the excitation/inhibition (E/I) ratio (Larsen et al., 2022; S. Zhang et al., 2024) using data from the Philadelphia Neurodevelopment Cohort (PNC) dataset (Satterthwaite et al., 2014; Calkins et al., 2015). The DELSSOME models were not retrained using the PNC dataset; instead, they remained identical to those employed in the HCP dataset to show their generalizability.

Initially, we hoped to confirm the previously observed decline in E/I ratio during developmental stages (S. Zhang et al., 2024) could be replicated by DELSSOME CMA-ES. In this experiment, we used the same setup as the previous work (S. Zhang et al., 2024). The cohort in PNC, comprising 885 participants, was stratified into 29 age groups and evenly split into training and validation sets for each group. We optimized local circuit parameters employing the DELSSOME CMA-ES which consisted of 100 DELSSOME evaluation iterations. Subsequently, 500 candidate parameter sets were generated and evaluated, with the parameter set exhibiting the lowest validation cost utilized to estimate regional E/I ratios across the cortex.

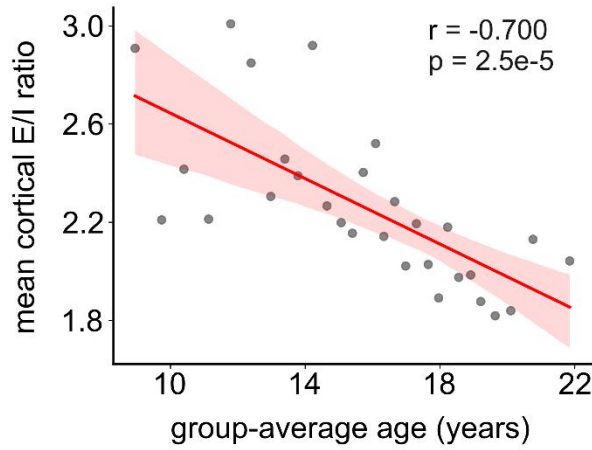
Consistent with our previous work, we observed a consistent decline in mean cortical E/I ratio throughout childhood and adolescence (**Figure 7A**, $r = -0.700$, $p = 2.5 \times 10^{-5}$), a trend observed across all cortical regions with statistical significance (FDR $q < 0.05$), compared to the results from Euler CMA-ES (**Figure 7B**). Furthermore, this reduction in E/I ratio demonstrated a spatial gradient, with sensory-motor regions exhibiting a more pronounced rate of decrease (i.e., a more negative age slope) compared to association networks (**Figure 7C, 7D**). The 100-region homotopic parcellation was also utilized and similar patterns were observed (Figure S3).

For cognitive analysis, same as our previous work (S. Zhang et al., 2024), we employed an established metric of overall accuracy and divided participants into 14 high-performance and 14 low-performance groups. Each high-performance group was age-matched to a corresponding low-performance group (**Figure 8A, 8B**). We utilized the same DELSSOME CMA-ES methodology as in the developmental analysis. Subsequently, E/I ratios were estimated and compared between high- and low-performance groups.

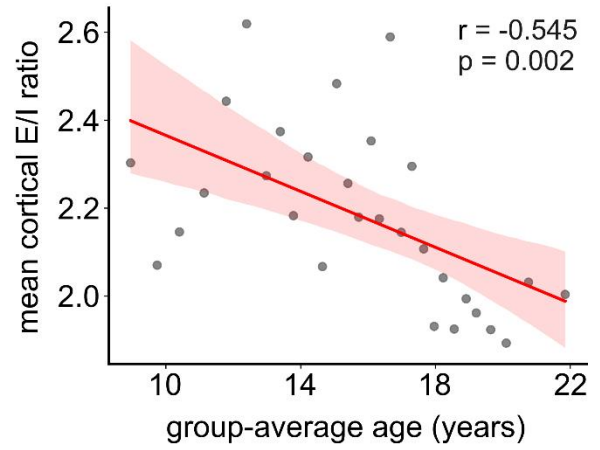
DELSSOME CMA-ES successfully replicated the previous finding that the high-performance group exhibited significantly lower mean cortical E/I ratio compared to the low-

performance group (**Figure 8C**, $p = 5.1 \times 10^{-3}$). Additionally, E/I ratio differences between low- and high-performance groups were more pronounced in transmodal regions compared to sensory-motor regions (**Figure 8E**, all FDR $q < 0.05$), which was consistent with our previous work (**Figure 8D, 8F**). We also applied the 100-region homotopic parcellation and showed similar results (Figure S4).

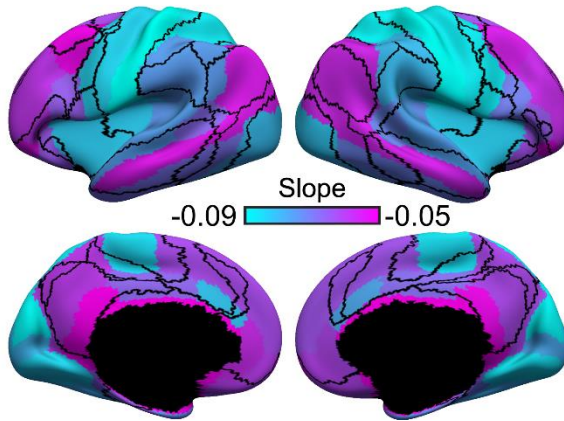
(A) Overall age effects (DELSSOME)



(B) Overall age effects (Euler)



(C) Slope bet. E/I ratio & age (DELSSOME)



(D) Slope bet. E/I ratio & age (Euler)

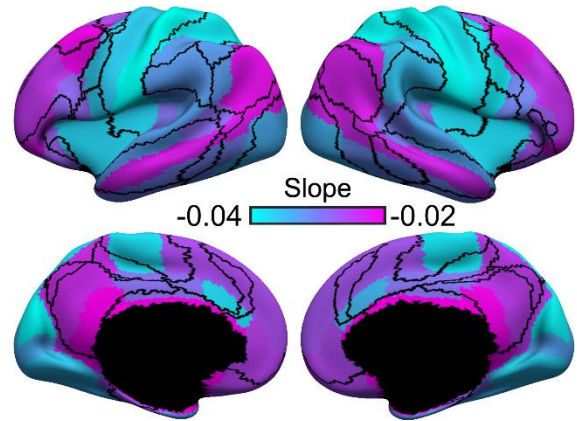


Figure 7. DELSSOME CMA-ES replicates E/I ratio decline during development. (A) (B) Mean cortical E/I ratio estimated by DELSSOME CMA-ES shows consistent decline as Euler CMA-ES. Participants in older age groups exhibited lower E/I ratio. 29 dots in the scatter plots corresponds to 29 age groups. The shaded area depicts 95% confidence interval of the linear relationship. (C) (D) Spatial distribution of linear regression slope between regional E/I ratio and age from DELSSOME CMA-ES are consistent with that from Euler CMA-ES. The values represent the rate of E/I ratio changes during development. All slopes are negative and significant (FDR $q < 0.05$).

These results underscore the robustness of the DELSSOME CMA-ES approach in replicating previous findings related to E/I ratio dynamics during development and cognitive processes, providing further validation of its utility in neuroscientific investigations.

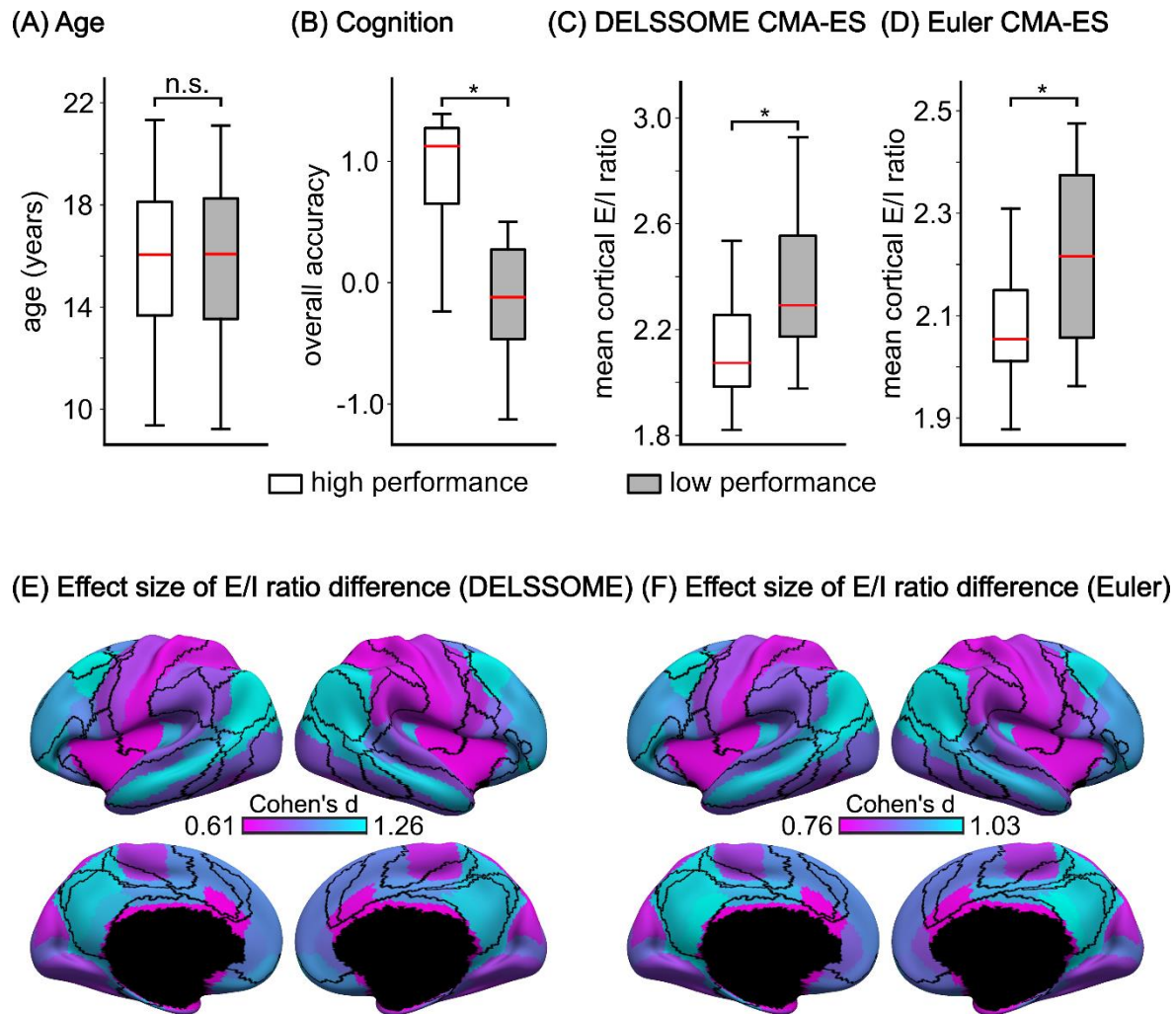


Figure 8. DELSSOME CMA-ES replicates the effect size of E/I ratio differences between high and low cognitive groups. (A) Boxplots of age, (B) ‘overall accuracy’ and (C) (D) mean cortical E/I ratio of high-performance and low-performance (overall accuracy) groups estimated by DELSSOME CMA-ES and Euler CMA-ES respectively. The mean cortical E/I ratio of the high-performance group was significantly lower than that of the low-performance group (FDR $q < 0.05$). (E) (F) Spatial distribution of effect size of regional E/I ratio difference between high-performance and low-performance groups estimated by DELSSOME CMA-ES and Euler CMA-ES respectively. All effect sizes were significant after FDR correction with $q < 0.05$.

4 Discussion

In this work, we proposed DELSSOME (DEep Learning for Surrogate Statistics Optimization in MEan field modeling), which showcased the feasibility of employing deep learning models to capture surrogate statistics for parameter optimization in large-scale biophysical circuit models. For the currently used large-scale biophysical model, our DELSSOME models consisted of two components: the DELSSOME out-of-range classifier and the DELSSOME loss predictor. By taking in local circuit parameters and structural connectivity (SC), the DELSSOME out-of-range classifier could accurately filter local circuit parameters likely to produce fMRI data beyond predefined ranges. The DELSSOME loss predictor directly computed the disagreement between simulated and empirical functional connectivity (FC) and the histogram of FC dynamics (FCD), without generating simulated fMRI data. Our results demonstrated strong alignment between predicted and ground truth loss values generated by Euler integration, affirming the effectiveness of the DELSSOME models. Further, the DELSSOME models were proved to successfully speed up the parameter optimization process. Integration of the DELSSOME models into the CMA-ES workflow allowed us to skip the step of simulating fMRI data, achieving a remarkable 500,000% speedup without compromising accuracy with the HCP dataset. Moreover, by applying the DELSSOME models to the PNC dataset, we confirmed their ability to retain biological information, as evidenced by the consistent findings with prior work regarding the Excitation/Inhibition (E/I) ratio and its association with cognitive ability (S. Zhang et al., 2024).

The embeddings generated by the multiple layer perceptrons (MLPs) in our neural network models served as surrogate statistics for predicting simulated fMRI data and assessing agreement between simulated and empirical fMRI data. These embeddings encapsulated abstract high-dimensional information from local circuit parameters, SC, FC, and FCD. Specifically, the surrogate statistics derived from local circuit parameters and SC encoded not only their features but also information regarding the differential equations in our large-scale biophysical model. Utilizing the embeddings, the DELSSOME out-of-range classifier extracted firing rate information, while the DELSSOME loss predictor inferred FC and the histogram of FCD in simulated fMRI data. By integrating these embeddings with those derived from empirical FC and FCD, the DELSSOME loss predictor could compute the loss terms pertaining to simulated FC and FCD compared to empirical counterparts.

The use of embeddings for local circuit parameters, SC, empirical FC, and the histogram of FCD were all critical in our approach, aligning with the requirements of the large-scale biophysical model and the evaluation process involving CMA-ES. In the large-scale biophysical model, local circuit parameters and SC matrices were essential for simulating fMRI data accurately. After generating simulated fMRI data, in the CMA-ES evaluation process, empirical FC and FCD embeddings were indispensable for assessing the agreement between simulated and empirical fMRI data. In our study, we employed a high-dimensional hidden space to align and integrate the embeddings of local circuit parameters, SC, FC, and the histogram of FCD. This alignment and integration within the same high-dimensional space were crucial for ensuring compatibility and facilitating meaningful analysis across different aspects of the biophysical model. The capability to align these embeddings within the same space was made possible by the inherent properties of the embedding space itself (He et al., 2022; Assran et al., 2023; Xiong et al., 2024). This concept paralleled previous methodologies like CLIP (Contrastive Language-Image Pre-training) (Radford et al., 2021), which employed a high-dimensional hidden space to align image and natural language embeddings. By leveraging a shared embedding space, we enabled direct comparison and integration of information across diverse components of the biophysical model. It is important to note that integrating information directly in the original space rather than in the embedding space would present significant drawbacks. Without the alignment provided by the shared embedding space, the different components would not be directly comparable and integration would be inherently complex and error-prone. Thus, the use of the high-dimensional hidden space facilitated integration and analysis of information across various components of the biophysical model, enhancing the interpretability and utility of the deep learning models. To implement this integration of embeddings from different matrices, we chose the addition operation rather than concatenation, a strategy akin to integrating positional encoding and word encoding in Transformer models (Vaswani et al., 2017; Devlin et al., 2019). Our approach underscored the versatility and effectiveness of leveraging embeddings to represent complex relationships and features, aligning with the broader trend in machine learning methodologies.

The mechanism behind the fast performance of DELSSOME CMA-ES lied in the usage of deep neural networks. The SC, FC, and FCD matrices for each pair of parameters could be transformed into the aforementioned embeddings. These embeddings were then decoded to directly output the loss terms ($1-r$, d , KS). Unlike traditional methods that relied on Euler simulations to generate time series and then calculated the loss terms, the

DELSSOME model replaced the time-consuming Euler simulation with a deep learning model forward pass, which took approximately 0.15 seconds compared to 750 seconds for Euler simulation when using 68 Desikan–Killiany regions of interest (ROIs). This significant reduction in computation time was the reason why DELSSOME CMA-ES greatly accelerated the optimization process for biophysical model local circuit parameters. It may seem counterintuitive that DELSSOME CMA-ES could achieve results comparable to or even numerically better than Euler CMA-ES. As shown in Figure 5, the scatter plot indicated that the DELSSOME predictor did not perfectly predict loss terms and exhibited significant deviations from the ground truth losses obtained by Euler simulation for some points. This discrepancy might be attributed to noise or possible degeneracy in each Euler simulation. Degeneracy is common in many optimization problems and biological systems (Dembo & Klincewicz, 1985; Edelman & Gally, 2001; J. Zhang et al., 2016). It occurs when two different sets of parameters yield the same loss, representing two local minima. However, these parameter sets often have distinct biophysical meanings. Nonetheless, during the DELSSOME CMA-ES optimization process, the predictor effectively captured the trend of optimizing parameters. This effect was seen in the validation processes of the parameter estimation workflow, where local circuit parameters generated by DELSSOME CMA-ES were input to the biophysical model for validation, and the validation losses showed a clear trend of decline (Figure S5). We hypothesized that DELSSOME CMA-ES generated a "clean" set of parameters, which was further reflected in the more pronounced trend exhibited by DELSSOME CMA-ES in the E/I ratio age effect in the PNC dataset experiments.

Despite the strong performance of DELSSOME models in FIC Euler loss prediction, our parcellation resolution is limited. In our study, we only utilized Desikan-Killiany 68-ROI and Yan 100-ROI homotopic parcellations (Yan et al., 2023). The bottleneck in our methodology was the dataset generation procedure, where the time required greatly scaled with the resolution.

Future work will focus on developing individual-level DELSSOME models. Currently, we have only performed group-level FIC Euler loss predictions. Individual-level predictions could reveal nuanced biophysical information, representing an important area in future research.

In summary, our work addressed key challenges in large-scale biophysical modeling by significantly accelerating model inversion, thus expediting computational research and facilitating more time-consuming analyses such as permutation tests. Additionally, the

embeddings in our models held promise for capturing novel biophysical patterns and assessing the regional impact of biophysical parameters and matrices.

Acknowledgements

Our research is supported by the NUS Yong Loo Lin School of Medicine (NUHSRO/2020/124/TMR/LOA), the Singapore National Medical Research Council (NMRC) LCG (OFLCG19May-0035), NMRC CTG-IIT (CTGIIT23jan-0001), NMRC STaR (STaR20nov-0003), Singapore Ministry of Health (MOH) Centre Grant (CG21APR1009), the Temasek Foundation (TF2223-IMH-01), and the United States National Institutes of Health (R01MH120080 & R01MH133334). Any opinions, findings and conclusions or recommendations expressed in this material are those of the authors and do not reflect the views of the Singapore NMRC, MOH or Temasek Foundation.

5 Appendix

5.1 Parametric feedback inhibition control (pFIC) model

The feedback inhibition control (FIC) model (Deco et al., 2014) was derived from the mean field reduction of spiking neuronal network models (Brunel & Wang, 2001; Wong & Wang, 2006). The detailed derivation of the FIC model can be found in a previous study (Deco et al., 2014). The differential equations describing neuronal activities of the j -th cortical region are shown below:

$$I_j^{(E)} = W_E I_0 + w_{EE} J_{NMDA} S_j^{(E)} + G J_{NMDA} \sum_k C_{jk} S_k^{(E)} - w_{IE} S_j^{(I)} \quad (1)$$

$$I_j^{(I)} = W_I I_0 + w_{EI} J_{NMDA} S_j^{(E)} - w_{II} S_j^{(I)} \quad (2)$$

$$r_j^{(E)} = \phi(I_j^{(E)}) = \frac{a_E I_j^{(E)} - b_E}{1 - \exp(-d_E (a_E I_j^{(E)} - b_E))} \quad (3)$$

$$r_j^{(I)} = \phi(I_j^{(I)}) = \frac{a_I I_j^{(I)} - b_I}{1 - \exp(-d_I (a_I I_j^{(I)} - b_I))} \quad (4)$$

$$\frac{dS_j^{(E)}}{dt} = -\frac{S_j^{(E)}}{\tau_E} + (1 - S_j^{(E)}) \gamma r_j^{(E)} + \sigma v_j(t) \quad (5)$$

$$\frac{dS_j^{(I)}}{dt} = -\frac{S_j^{(I)}}{\tau_I} + r_j^{(I)} + \sigma v_j(t) \quad (6)$$

where S , r , and I denote synaptic gating variables, firing rate, and synaptic currents respectively. The superscripts E and I represent the excitatory and inhibitory neuronal populations respectively.

The local circuit parameters, including w_{EE} (excitatory-to-excitatory recurrent connection strength), w_{EI} (excitatory-to-inhibitory connection strength), σ (noise amplitude) and G (global SC scaling constant) are unspecified and will be inferred by fitting to empirical fMRI data.

Building upon our prior research (S. Zhang et al., 2024), equations 1 to 6 were used to simulate the time courses of excitatory and inhibitory synaptic gating variables ($S_j^{(E)}$ and $S_j^{(I)}$) of each ROI with a fixed local circuit parameter set. The regional E/I ratio was defined as the average temporal ratio between $S_j^{(E)}$ and $S_j^{(I)}$. The mean cortical E/I ratio was then derived from averaging regional E/I ratios across all cortical ROIs. Additionally, the simulated excitatory synaptic gating variables ($S_j^{(E)}$) were inputted into the Balloon-Windkessel hemodynamic model to generate fMRI BOLD signals (Stephan et al., 2007; Deco et al., 2014). The simulated fMRI BOLD signals were utilized to generate simulated static FC and FCD.

References

- Assran, M., Duval, Q., Misra, I., Bojanowski, P., Vincent, P., Rabbat, M., LeCun, Y., & Ballas, N. (2023). Self-supervised learning from images with a joint-embedding predictive architecture. *Proceedings of the IEEE/CVF Conference on Computer Vision and Pattern Recognition*, 15619–15629.
http://openaccess.thecvf.com/content/CVPR2023/html/Assran_Self-Supervised_Learning_From_Images_With_a_Joint-Embedding_Predictive_Architecture_CVPR_2023_paper.html
- Brunel, N., & Wang, X.-J. (2001). Effects of Neuromodulation in a Cortical Network Model of Object Working Memory Dominated by Recurrent Inhibition. *Journal of Computational Neuroscience*, 11(1), 63–85.
<https://doi.org/10.1023/A:1011204814320>
- Burt, J. B., Demirtaş, M., Eckner, W. J., Navejar, N. M., Ji, J. L., Martin, W. J., Bernacchia, A., Anticevic, A., & Murray, J. D. (2018). Hierarchy of transcriptomic specialization across human cortex captured by structural neuroimaging topography. *Nature Neuroscience*, 21(9), 1251–1259. <https://doi.org/10.1038/s41593-018-0195-0>
- Calkins, M. E., Merikangas, K. R., Moore, T. M., Burstein, M., Behr, M. A., Satterthwaite, T. D., Ruparel, K., Wolf, D. H., Roalf, D. R., Mentch, F. D., Qiu, H., Chiavacci, R., Connolly, J. J., Sleiman, P. M. A., Gur, R. C., Hakonarson, H., & Gur, R. E. (2015). The Philadelphia Neurodevelopmental Cohort: Constructing a deep phenotyping collaborative. *Journal of Child Psychology and Psychiatry*, 56(12), 1356–1369.
<https://doi.org/10.1111/jcpp.12416>

- Cardin, J. A., Carlén, M., Meletis, K., Knoblich, U., Zhang, F., Deisseroth, K., Tsai, L.-H., & Moore, C. I. (2009). Driving fast-spiking cells induces gamma rhythm and controls sensory responses. *Nature*, 459(7247), 663–667.
- De Kock, C. P. J., & Sakmann, B. (2008). High frequency action potential bursts (≥ 100 Hz) in L2/3 and L5B thick tufted neurons in anaesthetized and awake rat primary somatosensory cortex. *The Journal of Physiology*, 586(14), 3353–3364. <https://doi.org/10.1113/jphysiol.2008.155580>
- Deco, G., Kringelbach, M. L., Arnatkeviciute, A., Oldham, S., Sabaroedin, K., Rogasch, N. C., Aquino, K. M., & Fornito, A. (2021). Dynamical consequences of regional heterogeneity in the brain's transcriptional landscape. *Science Advances*, 7(29), eabf4752. <https://doi.org/10.1126/sciadv.abf4752>
- Deco, G., Ponce-Alvarez, A., Hagmann, P., Romani, G. L., Mantini, D., & Corbetta, M. (2014). How Local Excitation-Inhibition Ratio Impacts the Whole Brain Dynamics. *Journal of Neuroscience*, 34(23), 7886–7898. <https://doi.org/10.1523/JNEUROSCI.5068-13.2014>
- Deco, G., Ponce-Alvarez, A., Mantini, D., Romani, G. L., Hagmann, P., & Corbetta, M. (2013). Resting-state functional connectivity emerges from structurally and dynamically shaped slow linear fluctuations. *Journal of Neuroscience*, 33(27), 11239–11252.
- Dembo, R. S., & Klincewicz, J. G. (1985). Dealing with degeneracy in reduced gradient algorithms. *Mathematical Programming*, 31(3), 357–363. <https://doi.org/10.1007/BF02591957>
- Demirtaş, M., Burt, J. B., Helmer, M., Ji, J. L., Adkinson, B. D., Glasser, M. F., Van Essen, D. C., Sotiropoulos, S. N., Anticevic, A., & Murray, J. D. (2019). Hierarchical heterogeneity across human cortex shapes large-scale neural dynamics. *Neuron*, 101(6), 1181–1194.
- Desikan, R. S., Ségonne, F., Fischl, B., Quinn, B. T., Dickerson, B. C., Blacker, D., Buckner, R. L., Dale, A. M., Maguire, R. P., & Hyman, B. T. (2006). An automated labeling system for subdividing the human cerebral cortex on MRI scans into gyral based regions of interest. *Neuroimage*, 31(3), 968–980.
- Devlin, J., Chang, M.-W., Lee, K., & Toutanova, K. (2019). *BERT: Pre-training of Deep Bidirectional Transformers for Language Understanding* (arXiv:1810.04805). arXiv. <https://doi.org/10.48550/arXiv.1810.04805>
- Edelman, G. M., & Gally, J. A. (2001). Degeneracy and complexity in biological systems. *Proceedings of the National Academy of Sciences of the United States of America*, 98(24), 13763–13768. <https://doi.org/10.1073/pnas.231499798>
- Froudust-Walsh, S., Bliss, D. P., Ding, X., Rapan, L., Niu, M., Knoblauch, K., Zilles, K., Kennedy, H., Palomero-Gallagher, N., & Wang, X.-J. (2021). A dopamine gradient controls access to distributed working memory in the large-scale monkey cortex. *Neuron*, 109(21), 3500–3520.
- Ghosh, A., Rho, Y., McIntosh, A. R., Kötter, R., & Jirsa, V. K. (2008). Noise during rest enables the exploration of the brain's dynamic repertoire. *PLoS Computational Biology*, 4(10), e1000196.
- Glasser, M. F., Sotiropoulos, S. N., Wilson, J. A., Coalson, T. S., Fischl, B., Andersson, J. L., Xu, J., Jbabdi, S., Webster, M., & Polimeni, J. R. (2013). The minimal preprocessing pipelines for the Human Connectome Project. *Neuroimage*, 80, 105–124.
- Glasser, M. F., & Van Essen, D. C. (2011). Mapping human cortical areas in vivo based on myelin content as revealed by T1-and T2-weighted MRI. *Journal of Neuroscience*, 31(32), 11597–11616.

- Goulas, A., Changeux, J.-P., Wagstyl, K., Amunts, K., Palomero-Gallagher, N., & Hilgetag, C. C. (2021). The natural axis of transmitter receptor distribution in the human cerebral cortex. *Proceedings of the National Academy of Sciences*, 118(3), e2020574118. <https://doi.org/10.1073/pnas.2020574118>
- Hansen, E. C., Battaglia, D., Spiegler, A., Deco, G., & Jirsa, V. K. (2015). Functional connectivity dynamics: Modeling the switching behavior of the resting state. *Neuroimage*, 105, 525–535.
- Hansen, N. (2006). The CMA Evolution Strategy: A Comparing Review. In J. A. Lozano, P. Larrañaga, I. Inza, & E. Bengoetxea (Eds.), *Towards a New Evolutionary Computation* (Vol. 192, pp. 75–102). Springer Berlin Heidelberg. https://doi.org/10.1007/3-540-32494-1_4
- He, K., Chen, X., Xie, S., Li, Y., Dollár, P., & Girshick, R. (2022). Masked autoencoders are scalable vision learners. *Proceedings of the IEEE/CVF Conference on Computer Vision and Pattern Recognition*, 16000–16009. https://openaccess.thecvf.com/content/CVPR2022/html/He_Masked_Autoencoders_Are_Scalable_Vision_Learners_CVPR_2022_paper
- Honey, C. J., Kötter, R., Breakspear, M., & Sporns, O. (2007). Network structure of cerebral cortex shapes functional connectivity on multiple time scales. *Proceedings of the National Academy of Sciences*, 104(24), 10240–10245. <https://doi.org/10.1073/pnas.0701519104>
- Honey, C. J., Sporns, O., Cammoun, L., Gigandet, X., Thiran, J. P., Meuli, R., & Hagmann, P. (2009). Predicting human resting-state functional connectivity from structural connectivity. *Proceedings of the National Academy of Sciences*, 106(6), 2035–2040. <https://doi.org/10.1073/pnas.0811168106>
- Huntenburg, J. M., Bazin, P.-L., & Margulies, D. S. (2018). Large-scale gradients in human cortical organization. *Trends in Cognitive Sciences*, 22(1), 21–31.
- Kong, X., Kong, R., Orban, C., Wang, P., Zhang, S., Anderson, K., Holmes, A., Murray, J. D., Deco, G., van den Heuvel, M., & Yeo, B. T. T. (2021). Sensory-motor cortices shape functional connectivity dynamics in the human brain. *Nature Communications*, 12(1), Article 1. <https://doi.org/10.1038/s41467-021-26704-y>
- Kringelbach, M. L., & Deco, G. (2020). Brain states and transitions: Insights from computational neuroscience. *Cell Reports*, 32(10). [https://www.cell.com/cell-reports/fulltext/S2211-1247\(20\)31117-7](https://www.cell.com/cell-reports/fulltext/S2211-1247(20)31117-7)
- Lam, N. H., Borduqui, T., Hallak, J., Roque, A., Anticevic, A., Krystal, J. H., Wang, X.-J., & Murray, J. D. (2022). Effects of altered excitation-inhibition balance on decision making in a cortical circuit model. *Journal of Neuroscience*, 42(6), 1035–1053.
- Larsen, B., Cui, Z., Adebimpe, A., Pines, A., Alexander-Bloch, A., Bertolero, M., Calkins, M. E., Gur, R. E., Gur, R. C., Mahadevan, A. S., Moore, T. M., Roalf, D. R., Seidlitz, J., Sydnor, V. J., Wolf, D. H., & Satterthwaite, T. D. (2022). A developmental reduction of the excitation:inhibition ratio in association cortex during adolescence. *Science Advances*, 8(5), eabj8750. <https://doi.org/10.1126/sciadv.abj8750>
- Leonardi, N., & Van De Ville, D. (2015). On spurious and real fluctuations of dynamic functional connectivity during rest. *Neuroimage*, 104, 430–436.
- Margulies, D. S., Ghosh, S. S., Goulas, A., Falkiewicz, M., Huntenburg, J. M., Langs, G., Bezgin, G., Eickhoff, S. B., Castellanos, F. X., Petrides, M., Jefferies, E., & Smallwood, J. (2016). Situating the default-mode network along a principal gradient of macroscale cortical organization. *Proceedings of the National Academy of Sciences*, 113(44), 12574–12579. <https://doi.org/10.1073/pnas.1608282113>
- Paszke, A., Gross, S., Massa, F., Lerer, A., Bradbury, J., Chanan, G., Killeen, T., Lin, Z., Gimelshein, N., & Antiga, L. (2019). Pytorch: An imperative style, high-performance

- deep learning library. *Advances in Neural Information Processing Systems*, 32. <https://proceedings.neurips.cc/paper/2019/hash/bdbca288fee7f92f2bfa9f7012727740-Abstract.html>
- Radford, A., Kim, J. W., Hallacy, C., Ramesh, A., Goh, G., Agarwal, S., Sastry, G., Askell, A., Mishkin, P., & Clark, J. (2021). Learning transferable visual models from natural language supervision. *International Conference on Machine Learning*, 8748–8763. <http://proceedings.mlr.press/v139/radford21a>
- Satterthwaite, T. D., Elliott, M. A., Ruparel, K., Loughhead, J., Prabhakaran, K., Calkins, M. E., Hopson, R., Jackson, C., Keefe, J., & Riley, M. (2014). Neuroimaging of the Philadelphia neurodevelopmental cohort. *Neuroimage*, 86, 544–553.
- Shine, J. M., Müller, E. J., Munn, B., Cabral, J., Moran, R. J., & Breakspear, M. (2021). Computational models link cellular mechanisms of neuromodulation to large-scale neural dynamics. *Nature Neuroscience*, 24(6), 765–776. <https://doi.org/10.1038/s41593-021-00824-6>
- Singh, M. F., Braver, T. S., Cole, M. W., & Ching, S. (2020). Estimation and validation of individualized dynamic brain models with resting state fMRI. *NeuroImage*, 221, 117046. <https://doi.org/10.1016/j.neuroimage.2020.117046>
- Smith, R. E., Tournier, J.-D., Calamante, F., & Connelly, A. (2012). Anatomically-constrained tractography: Improved diffusion MRI streamlines tractography through effective use of anatomical information. *Neuroimage*, 62(3), 1924–1938.
- Smith, R. E., Tournier, J.-D., Calamante, F., & Connelly, A. (2015). SIFT2: Enabling dense quantitative assessment of brain white matter connectivity using streamlines tractography. *Neuroimage*, 119, 338–351.
- Stephan, K. E., Weiskopf, N., Drysdale, P. M., Robinson, P. A., & Friston, K. J. (2007). Comparing hemodynamic models with DCM. *Neuroimage*, 38(3), 387–401.
- Tournier, J. D., Calamante, F., & Connelly, A. (2010). Improved probabilistic streamlines tractography by 2nd order integration over fibre orientation distributions. *Proceedings of the International Society for Magnetic Resonance in Medicine*, 1670. <https://archive.ismrm.org/2010/1670.html>
- Tournier, J.-D., Smith, R., Raffelt, D., Tabbara, R., Dhollander, T., Pietsch, M., Christiaens, D., Jeurissen, B., Yeh, C.-H., & Connelly, A. (2019). MRtrix3: A fast, flexible and open software framework for medical image processing and visualisation. *Neuroimage*, 202, 116137.
- Trakoshis, S., Martínez-Cañada, P., Rocchi, F., Canella, C., You, W., Chakrabarti, B., Ruigrok, A. N., Bullmore, E. T., Suckling, J., & Markicevic, M. (2020). Intrinsic excitation-inhibition imbalance affects medial prefrontal cortex differently in autistic men versus women. *Elife*, 9, e55684.
- Van Essen, D. C., Smith, S. M., Barch, D. M., Behrens, T. E., Yacoub, E., Ugurbil, K., & Consortium, W.-M. H. (2013). The WU-Minn human connectome project: An overview. *Neuroimage*, 80, 62–79.
- Vaswani, A., Shazeer, N., Parmar, N., Uszkoreit, J., Jones, L., Gomez, A. N., Kaiser, \Lukasz, & Polosukhin, I. (2017). Attention is all you need. *Advances in Neural Information Processing Systems*, 30. <https://proceedings.neurips.cc/paper/7181-attention-is-all>
- Wang, P., Kong, R., Kong, X., Liégeois, R., Orban, C., Deco, G., van den Heuvel, M. P., & Thomas Yeo, B. T. (2019). Inversion of a large-scale circuit model reveals a cortical hierarchy in the dynamic resting human brain. *Science Advances*, 5(1), eaat7854. <https://doi.org/10.1126/sciadv.aat7854>
- Wilson, F. A., O'Scalaidhe, S. P., & Goldman-Rakic, P. S. (1994). Functional synergism between putative gamma-aminobutyrate-containing neurons and pyramidal neurons in

- prefrontal cortex. *Proceedings of the National Academy of Sciences*, 91(9), 4009–4013. <https://doi.org/10.1073/pnas.91.9.4009>
- Wong, K.-F., & Wang, X.-J. (2006). A recurrent network mechanism of time integration in perceptual decisions. *Journal of Neuroscience*, 26(4), 1314–1328.
- Xiong, Y., Varadarajan, B., Wu, L., Xiang, X., Xiao, F., Zhu, C., Dai, X., Wang, D., Sun, F., & Iandola, F. (2024). Efficientsam: Leveraged masked image pretraining for efficient segment anything. *Proceedings of the IEEE/CVF Conference on Computer Vision and Pattern Recognition*, 16111–16121. https://openaccess.thecvf.com/content/CVPR2024/html/Xiong_EfficientSAM_Leveraged_Masked_Image_Pretraining_for_Efficient_Segment_Anything_CVPR_2024_paper.html
- Yan, X., Kong, R., Xue, A., Yang, Q., Orban, C., An, L., Holmes, A. J., Qian, X., Chen, J., & Zuo, X.-N. (2023). Homotopic local-global parcellation of the human cerebral cortex from resting-state functional connectivity. *NeuroImage*, 273, 120010.
- Zalesky, A., Fornito, A., Cocchi, L., Gollo, L. L., & Breakspear, M. (2014). Time-resolved resting-state brain networks. *Proceedings of the National Academy of Sciences*, 111(28), 10341–10346. <https://doi.org/10.1073/pnas.1400181111>
- Zhang, J., Kaess, M., & Singh, S. (2016). On degeneracy of optimization-based state estimation problems. *2016 IEEE International Conference on Robotics and Automation (ICRA)*, 809–816. <https://ieeexplore.ieee.org/abstract/document/7487211/>
- Zhang, S., Larsen, B., Sydnor, V. J., Zeng, T., An, L., Yan, X., Kong, R., Kong, X., Gur, R. C., Gur, R. E., Moore, T. M., Wolf, D. H., Holmes, A. J., Xie, Y., Zhou, J. H., Fortier, M. V., Tan, A. P., Gluckman, P., Chong, Y. S., ... Yeo, B. T. T. (2024). In vivo whole-cortex marker of excitation-inhibition ratio indexes cortical maturation and cognitive ability in youth. *Proceedings of the National Academy of Sciences*, 121(23), e2318641121. <https://doi.org/10.1073/pnas.2318641121>